# Electric Propulsion System Analysis Using Performance Maps

HONG-SU NAM DEC HAK-TAE LEE

Inha University, Incheon, Republic of Korea

This article presents a detailed methodology for the analysis and optimization of electric propulsion systems, using a comprehensive set of performance maps. By expressing critical performance metrics such as flight speed and climb rate, in addition to the component efficiencies as contour plots, this approach offers visual insights into the interactions of each component within the combined system. The methodology identified rotational speed and torque as the two common independent variables for computing efficiency maps for each component enabling unified approach for numerical solvers and visual validation of the solution within the multiple contour plots. A comparative analyses of different efficiency models are presented, complemented by experimental measurements to validate the proposed approach. The practical utility of this methodology is demonstrated through two specific use cases. In the first scenario, the optimal propeller is identified to achieve the maximum range for a given aircraft in a level flight. In the second scenario, a strategy involving repeated powered climbs and power-off glides is evaluated to determine its potential in further extending the flight range. In particular, the study shows that employing periodic flight strategies can enhance range as much as 40% compared to conventional approaches. The described methodology provides a robust framework applicable to the optimization of aircraft system, offering guidance for component selection and system integration, and mission strategies.

Received 23 October 2024; revised 17 January 2025; accepted 18 February 2025. Date of publication 24 February 2025; date of current version 11 August 2025.

DOI. No. 10.1109/TAES.2025.3544619

Refereeing of this contribution was handled by R. Meyer.

This work was supported in part by the National Research Foundation of Korea (NRF) through the Korea government (MSIT) under GrantRS-2023-00258573 and in part by the Data Driven Air Traffic Management through the Ministry of Land, Infrastructure, and Transport of the Korean Government under Grant RS-2021-KA163373.

Authors' address: Hong-Su Nam, Seok-Hwan Lee, and Hak-Tae Lee are with the Department of Aerospace Engineering and the Program in Aerospace Systems Convergence, Inha University, Incheon 21999, Republic of Korea, E-mail: (namhs501@inha.edu; seokhwan-lee@inha.edu; haktae.lee@inha.ac.kr). (Corresponding author: Hak-Tae Lee.)

0018-9251 © 2025 IEEE

#### NOMENCLATURE

 $\dot{h}$  Rate of climb.  $\eta_e$  ESC efficiency.  $\eta_m$  Motor efficiency.  $\eta_p$  Propeller efficiency.

 $\eta_{e-m}$  Combined ESC-motor efficiency.

 $\omega$  Rotational speed.  $\rho$  Air density.

 $C_D$  Total drag coefficient.  $C_L$  Lift coefficient.

 $C_P$  Propeller power coefficient.  $C_T$  Propeller thrust coefficient.

D Propeller diameter.  $d_R$  Aircraft range.  $E_b$  Battery energy.

 $f_{\text{PWM}}$  Pulsewidth modulation frequency.

 $i_0$  No-load current.  $i_b$  Battery output current.  $i_m$  Motor input current. J Advance ratio.

*k* Overall induced drag factor.

 $k_t$  Torque constant.

L Lift.

Rotational speed (Revolutions per second).

 $P_b$  Battery power.  $P_e$  ESC power.  $P_L$  Motor power loss.  $P_m$  Motor power.  $P_p$  Propeller power.  $P_{rc}$  Resistive loss.  $P_{sb}$  Standby power loss.

 $P_{sw}$  Switching loss. Q Torque.

 $Q_f$  Friction torque.

Motor internal resistance.

 $r_D$  Duty ratio.  $R_{ds,ON}$  Switch resistance. rpm Revolutions per minute. S Wing reference area.  $t_E$  Aircraft endurance.  $T_{sd}$  Switching delay.

V Forward flight speed.  $v_b$  Battery output voltage.  $v_m$  Motor input voltage. W Aircraft weight.

 $C_{DP}$  Parasite drag coefficient.

 $C_{L_{\min}}$  Lift coefficient at minimum drag coefficient.

AC Alternating current.

COTS Commercial off-the-shelf.

DC Direct current.

ECM Equivalent circuit model.

EECM Enhanced equivalent circuit model.

ESC Electronic speed control. LBM Loss build-up model.

#### I. INTRODUCTION

The propulsion system of an electric fixed wing aircraft has the following basic components: an airframe, propellers, electric motors, electronic speed controls (ESCs), and batteries. Electric propulsion systems have been widely used for smaller unmanned aircraft (UA). However, in recent years, many companies have started developing electric-powered manned aircraft [1], [2], [3]. Optimizing the selection of components for the required flight conditions is becoming increasingly important as the mismatched components can negatively impact the total efficiency of the system, resulting in difficulties in satisfying the mission requirements.

One of the fundamental difficulties of the propulsion system integration is that all components are tightly coupled, which requires solving system of nonlinear equations using a numerical solver or an optimizer. For a basic constant speed level flight, three conditions must be satisfied: lift must be equal to weight, thrust must be equal to drag, and the motor output torque must be equal to the propeller input torque. Another factor that makes the problem more complicated is that the airframe and the propeller performance characteristics are often provided in multiple lookup tables.

The efficiencies of each component, ESC, motor, and propeller, under a wide range of operating conditions have been studied extensively.

Gong and Verstraete [4] made measurements of commercial of-the-shelf (COTS) hobby grade ESCs and presented a 2-D regression model of the ESC efficiency using the voltage and current input of the ESCs. The low cost ESCs were more efficient at lower voltage and high current regions, and the maximum efficiencies were around 85%.

Equivalent circuit models (ECMs) [5], [6] have been widely used to model the motors. Attempts to increase the accuracy of the basic ECM by considering the second order electromagnetic effects and more realistic friction models are made. Larminie and Lowry [7] proposed a model for computing the motor efficiency by adding individual power losses such as iron loss and windage loss in addition to the copper loss and friction loss. Saemi and Benedict [8] developed a motor efficiency model that includes switching loss and harmonic loss, which can be obtained from a minimal set of manufacturer data to improve the ECM and presented comparison results with measurements. This study also developed an improved ESC and battery models to analyze the power system of quad-rotor drones.

As models tend to be less accurate, and as it is difficult to obtain all the required parameters from the manufacturer, some of the studies used measurement based approaches. McDonald [9] showed how to obtain a polynomial fit of the motor efficiency, called a positive polynomial loss model,

using a non-negative least-squares method over measurement data. Muzar and Lanteigne [10] calculated theoretical performance predictions for motors and propellers to select an appropriate motor-propeller combination and compared them with experimental results obtained from static thrust and torque tests. Lee et al. [11] developed a method to obtain ESC-motor combined efficiency contours by using a low cost reaction torque measurement device and by interpolating the measurement data of multiple propellers based on the approach of [10].

Battery discharge models are also investigated even though battery performance is generally less sensitive to the operational conditions compared to other electric propulsion components. Traub [12] investigated the relationship between battery capacity and performance, such as aircraft range and endurance. However, a constant total efficiency was assumed for the rest of the power system. Nam et al. [13] performed a chemistry simulation of a battery and discovered that the battery discharge characteristics of decreasing voltage and increasing current at a constant power draw do not negatively impact the ESC efficiency.

For the integration of the individual component into a total system, solver or optimizer-based approaches have been widely used. Duan et al. [14] proposed an optimizationbased design method using the improved parallel hybrid particle swarm optimization and differential evolution algorithm for the motor propeller system of a UA. The final output was the propeller geometry. Dai et al. [15] integrated a equivalent circuit motor model corrected for motor resistance with a simple ESC, propeller, and battery model to optimize the propulsion system of a multicopter. In addition, a method of finding the optimal product from the database was presented by estimating the main design parameters of each component. MacNeil et al. [16] designed the optimal propeller shape according to the operating point of a UA using a hybrid genetic algorithm-sequential quadratic programming optimization technique. Zhang et al. [17] designed and optimized the electric propulsion system of the quadrotor fixed-wing hybrid UA by considering its ability to reject wind disturbances in quadrotor mode. In this work, propellers were analyzed using a blade element momentum theory model. Though it is possible to obtain the optimized single point design based on the models that are utilized, it is not easy to obtain a broader insight of the propulsion system especially at off design conditions.

Performance contour or map-based approaches can provide a rich set of information about the system not only at a single point but at a wide range of two operating parameters used to construct the map. McDonald [18] plotted motor efficiency contours and propeller performance envelopes together on a plane represented by the rotational speed,  $\omega$ , in the x axis and torque, Q, in the y-axis ( $\omega$ -Q plane); however, did not utilize detailed propeller efficiency contours, because a variable pitch propeller was used. MacNeil et al. [16] presented engine efficiency contours, but it was used as an input to an optimizer. Duan et al. [14] presented a motor efficiency map and used the map in the optimization framework similar to [16]. Gong et al. [19]

described a procedure for testing the performance characteristics of an electric aircraft and introduced the contours for the forward flight speed on the  $\omega$ -Q plane.

Lee [20] introduced a methodology to plot the efficiency and other key parameter contours of motor, propeller, and airframe on a single plot on the  $\omega$ -Q plane. This work provided a holistic insight of an electric propulsion system in a visual form for a wide range of operating conditions. Nam et al. [21] improved [20] by adding the ESC model of [9] and a propeller efficiency model that are dependent on the rotational speed in addition to the advance ratio to reflect the impact of the Reynolds number. In this study, two ESCs, motors, and propellers, which yields a total of eight combinations are compared to demonstrate that the flight range can vary over 10% even though each component is similar to one another.

This article, an evolution of [21], presents the detailed process of constructing and using the efficiency contours of the ESC, motor, and propeller as well as the forward flight speed and thrust contours in the  $\omega$ -Q plane. For the airframe, climb rate contours are used. While explaining the efficiency contours, different ESC and motor efficiency models are presented, and some of the models are compared with the measurement data.

Two use cases are presented to highlight the importance of the propulsion system optimization. The first case evaluates eight different propellers to find the one that provides the longest range in steady level flight. The overall efficiency ranged from about 39%–45%. The second case investigates a repeated climb and power off glide flight strategy that utilizes the higher efficiency operating condition not at a level flight but at a certain climb rate. The results show that the range can increase by 40% by repeating climb and glide compared to the best steady level flight condition.

The proposed method provides an overview of the status of the propulsion system to the designers so that they can quickly identify if the propulsion system is well matched or what is required to improve the system. In addition, unifying the independent variables to rotational speed and torque for all the electric propulsion components makes the use of numerical solver or optimizer more intuitive and straightforward. The solution obtained by the optimizer can be cross validated with the contour maps to identify its positioning in the operational space.

The rest of this article is organized as follows. Section II presents the overview of an electric propulsion system as well as the analysis of the component efficiency using rotational speed and torque. In this section, several different models of ESCs and motors are presented and compared. Section III presents the results of the two use cases, which demonstrate the usefulness of the proposed approaches. Finally, Section IV concludes this article.

## II. ELECTRIC PROPULSION COMPONENTS

A general electric propulsion system is composed of a battery, an ESC, a motor, a propeller, and an airframe. Fig. 1 shows how the battery's electric power flows downstream

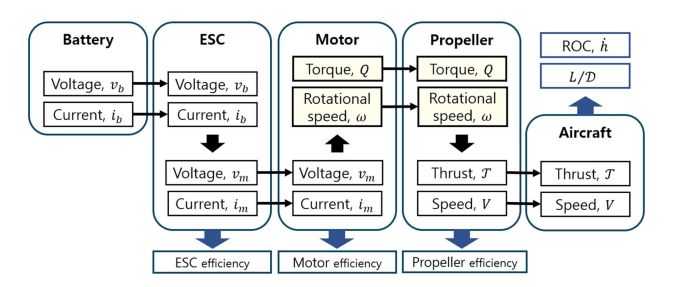


Fig. 1. Power transfer dynamics in the electric propulsion system.

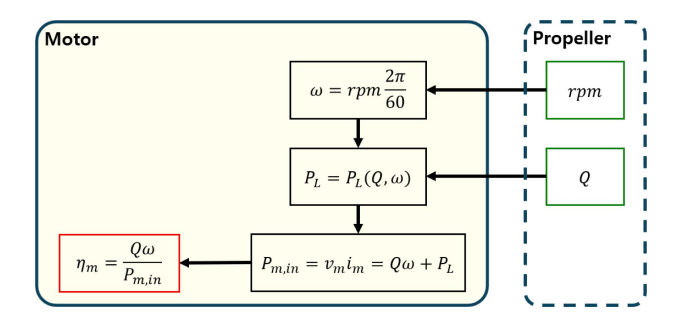


Fig. 2. Procedure for calculating the motor efficiency from given rpm and O.

while changing the form from electric power to mechanical power. The electric power output of the battery, represented by voltage and current is converted to different, typically modulating, voltage, and current by the ESC. The motor converts the electric power from the ESC to mechanical power represented by the rotational speed and torque outputs. Mechanical power output of the motor in the rotational form is converted to a linear form, represented by thrust and the speed of the airframe. During this flow,  $\omega$  and Q that link motor and propeller, which are in the middle of power transfer dynamics, are identified as the optimum two independent variables to analyze all four components in a common plot. Consequently, all the following analysis results are visualized in the  $\omega$ -Q plane.

#### A. Motor

Motor efficiency contours are commonly used in the  $\omega$ -Q plane. Efficiency can be calculated in terms of torque and rotational speed from the applied voltage,  $v_m$ , and current,  $i_m$ , to the motor, or it can be expressed in terms of the power loss,  $P_L$ , as shown in (1). The process of representing motor efficiency,  $\eta_m$ , on the  $\omega$ -Q plane is summarized in Fig. 2. At each grid point, the power loss,  $P_L$  is uniquely determined by the motor's  $\omega$  and output Q. Several different models of  $P_L$  are presented in the subsequent sections. The input power of the motor is calculated by adding  $P_L$  to the output power,  $Q\omega$ .  $\eta_m$ , can be calculated as follows:

$$\eta_m = \frac{P_{m,\text{out}}}{P_{m,\text{in}}} = \frac{Q\omega}{v_m i_m} = \frac{Q\omega}{Q\omega + P_L}.$$
(1)

There are typically two commonly used motor models, with the first being the ECM [5]. The ECM uses manufacturer-provided parameters such as no-load current,

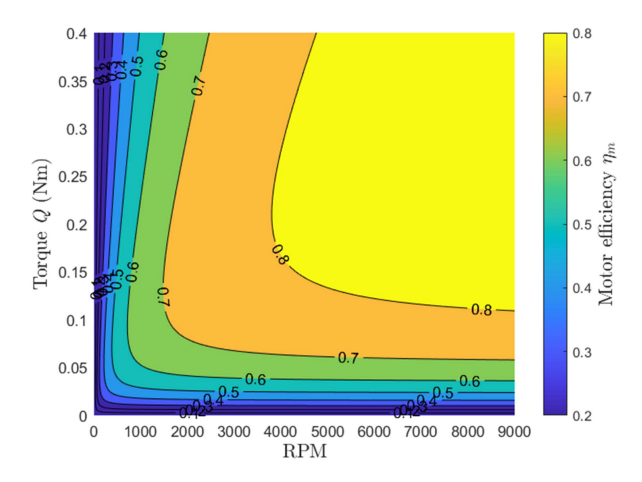


Fig. 3. Efficiency map of "AT2826-900KV" motor based on ECM.

TABLE I "AT2826-900KV" Motor Manufacturer Provided Data

Parameter	Value
No-load current, $i_0$	2.2 (A)
Internal resistance, $r$	$0.024 (\Omega)$
Torque constant, $k_t$	0.0106 (Vs)

 $i_0$ , internal resistance, r, and torque constant,  $k_t$ . In the simplest form of the ECM, the friction torque,  $Q_f$ , is assumed to be constant and calculated using (2) unless specified by the manufacturer. Power loss of the ECM,  $P_{L,\text{ECM}}$ , is expressed in (3). As can be seen from (3),  $P_{L,\text{ECM}}$  is a function of  $\omega$  and Q only and is a sum of the mechanical power loss due to friction and electric power loss due to resistivity

$$Q_f = k_t i_0 \tag{2}$$

$$P_{L,\text{ECM}} = Q_f \omega + r \left(\frac{Q + Q_f}{k_t}\right)^2. \tag{3}$$

The ECM is advantageous for providing an analytic motor model during the initial design stages. However, ECM tends to be inaccurate at large  $\omega$ s especially when the aerodynamic resistance torque on the rotor becomes nonnegligible. Fig. 3 shows the efficiency map of the "T-Motor AT2826-900KV" using the ECM and the manufacturer provided data [22] shown in Table I.

The second model is the loss build-up model (LBM), which is described in [7]. The LBM considers the motor's default power loss, iron loss, windage loss, copper loss, and friction loss. The total power loss  $P_{L, LBM}$  is expressed as shown in the following:

$$P_{LLBM} = c_0 + c_1 \omega + c_2 \omega^3 + c_3 Q^2. \tag{4}$$

Notable addition of the LBM compared with the ECM is the windage loss expressed as the  $\omega^3$  term in (4), which is missing in (3). However, to obtain proper values of the coefficients,  $c_i$ , measurement data are required. If the  $\omega$  and Q for the maximum efficiency are known, the coefficients can be found using the method described in [23]. Fig. 4 shows the efficiency map of the same motor as in Fig. 3 using LBM. As the manufacturer provided a table of test data [22],

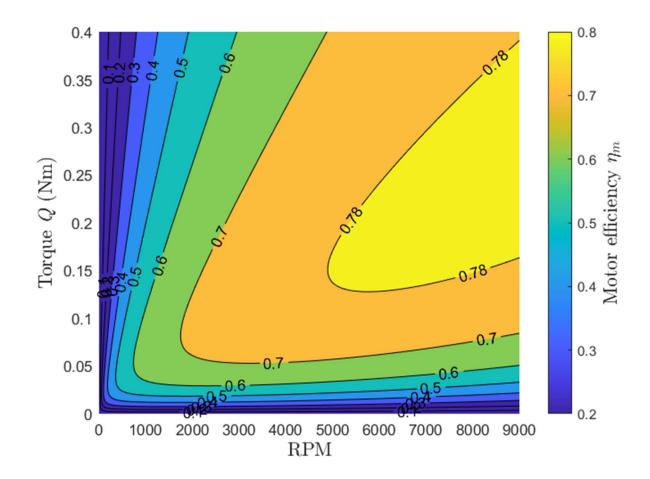


Fig. 4. Efficiency map of "AT2826-900KV" motor based on LBM and measurement data.

the  $\omega$  and Q that resulted in the maximum efficiency among the test cases are used. It should be noted that the test data may not encompass true maximum efficiency point. In addition, the given measurements are not the efficiency of the motor alone but rather the combined efficiency of ESC and motor. ESC efficiencies are discussed in the following section but Fig. 4 assumes the ESC efficiency is constant.

In addition to the two motor models previously described, more generalized power loss model in the form of (5) can be used if sufficient measurement data points are available. McDonald [9] referred to this model as the positive polynomial loss model (PLM) and described a method to fit the measurement data

$$P_{L,\text{PLM}} = \sum_{i=0}^{m_Q} \sum_{j=0}^{m_\omega} c_{i,j} Q^i \omega^j.$$
 (5)

The PLM is suitable when an analytically expressed model that closely matches the actual measurement data is desired. Without considering the physical significance, it is possible to obtain a close representation of the measurement data by adjusting the orders of  $\omega$  and Q,  $m_{\omega}$  and  $m_{Q}$ , respectively.

Saemi and Benedict [8] proposed an enhanced ECM (EECM) with additional correction factors so that the motor efficiency model can be obtained with the limited set of manufacturers published data but better matches the measurements. The power loss  $P_{L, \text{EECM}}$  is given by the following:

$$P_{L,\text{EECM}} = 0.1Q\omega + \frac{1}{r_D} \left\{ Q_f \omega + r \left( \frac{Q + Q_f}{k_t} \right)^2 \right\}$$
 (6)

where the duty ratio,  $r_D$ , is defined in the following:

$$r_D = \frac{k_t \omega}{v_b}. (7)$$

The duty ratio amplifies resistive and iron losses when  $r_D < 1$  to model harmonic distortion from modulating battery voltage,  $v_b$ , at partial throttle settings. A 10% penalty on the motor's output term reflects high-order iron losses. Similar

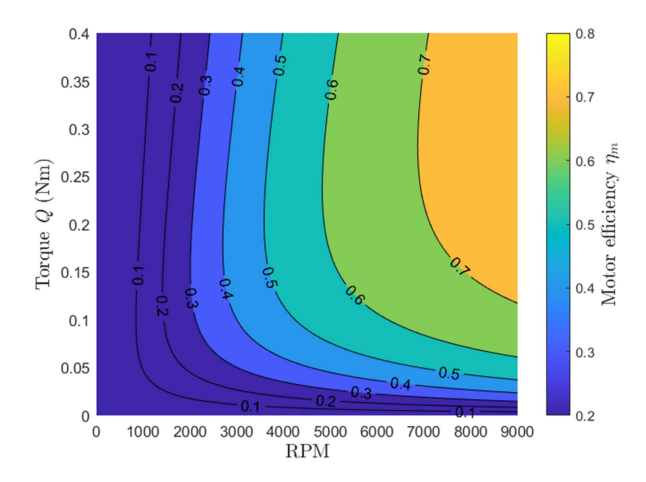


Fig. 5. Efficiency map of "AT2826-900KV" motor based on EECM.

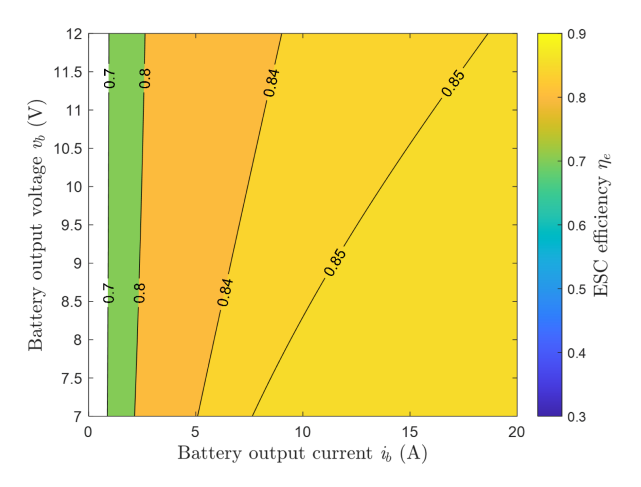


Fig. 6. Efficiency map of the "SuperBrain40" ESC in the  $v_b$ - $i_b$  plane. [4].

to the ECM, the EECM does not incorporate measurement data, but it provides motor efficiency as a function of  $\omega$  and Q using only the manufacturer-provided  $i_0$ , r,  $k_t$ , and  $v_b$ . Fig. 5 shows the efficiency map of the same motor using the EECM.

### B. ESC

The efficiencies of the COTS hobby grade ESCs are generally assumed to be between 80 and 90% under constant load conditions. Consequently, assuming a constant value for the ESC efficiency can be sufficient for analyzing electric propulsion systems [8]. However, Lee et al. [11] showed that the ESC with higher current rating is more efficient by testing two different ESCs from the same manufacturer with the same motor.

One of the few stand alone ESC efficiency models is presented by [4] as a functions of  $v_b$  and battery current,  $i_b$ , as shown in Fig. 6. The ESC efficiency,  $\eta_e$ , is defined as in the following:

$$\eta_e = \frac{P_{e,\text{out}}}{P_{e,\text{in}}} = \frac{v_m i_m}{v_b i_b}.$$
 (8)

To apply the strategies of this study,  $\eta_e$  needs to be converted to a function of Q and  $\omega$ . From (1), the ESC output

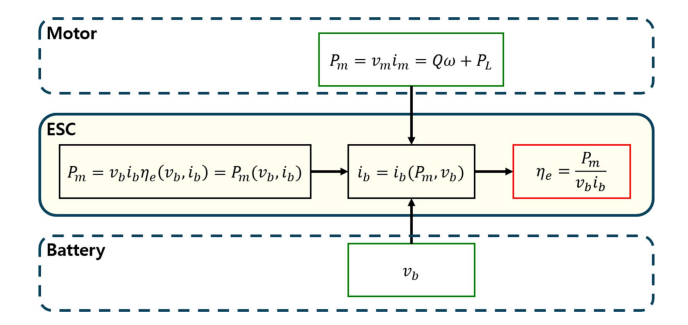


Fig. 7. Procedure for representing the ESC efficiency in the  $\omega$ -Q plane.

power can be expressed in terms of the motor input power,  $P_m$ , and the motor's characteristic power loss as shown in the following:

$$v_m i_m = v_b i_b \eta_e (v_b, i_b) = Q\omega + P_L (Q, \omega). \tag{9}$$

For a fixed  $v_b$ ,  $i_b$  can be found if Q and  $\omega$  are given by solving (9), which means  $i_b$  is obtained as a function of Q and  $\omega$  as shown in the following:

$$i_b = i_b(Q, \omega). \tag{10}$$

In conclusion,  $\eta_e$ , can be formulated as a function of Q and  $\omega$  as shown in the following, with a summary of this process illustrated in Fig. 7:

$$\eta_e = \eta_e(Q, \omega) = \frac{Q\omega + P_L(Q, \omega)}{v_b \cdot i_b(Q, \omega)}.$$
 (11)

The ESC efficiency model given in [4] accounts for conduction loss due to the inherent resistance of each component used in the switching circuit, switching loss incurred during the conversion of dc input power to the three-phase ac required by the brushless dc motor, and losses due to standby power. The model is given in the following as a function of  $v_b$  and  $i_b$ :

$$\eta_e = a_0 \frac{i_b^2}{v_b} + a_1 + a_2 \frac{1}{i_b} + a_3 \frac{1}{v_b}$$
 (12)

where  $a_1, a_2, a_3$ , and  $a_4$  are coefficients determined by fitting the measurement data of the specific ESC model. If (12) is plugged into (9), it is rearranged into a cubic equation in  $i_b$  as in (13). By solving the following,  $i_b$  as a function of Q and  $\omega$  as in (10) is found:

$$a_0 i_b^3 + (a_1 v_b + a_3) i_b + (a_2 v_b - Q\omega - P_L(Q, \omega)) = 0.$$
(13)

Using the "AT2312-1150KV" motor and a three cell lithium battery, which has a nominal voltage of 11.1 V, the efficiency contours of Fig. 6 are reconstructed in the  $\omega$ -Q plane, as presented in Figs. 8 and 9. Figs. 8 and 9 illustrate the efficiencies when the motor models EECM and LBM are used, respectively. This comparison shows that, even with the same ESC efficiency model in terms of  $v_b$  and  $i_b$ , the efficiency contours on the  $\omega$ -Q plane can show a significant difference depending on the motor model. Closer investigation reveals that the difference is small at higher  $\omega$  or Q regions where the motor tends to be more efficient.

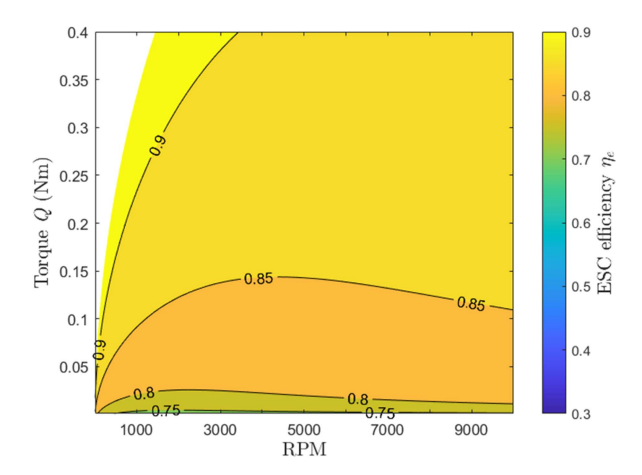


Fig. 8. Efficiency map of the "SuperBrain40" ESC with the EECM of the "AT2312-1150KV" motor in the  $\omega$ -Q plane.

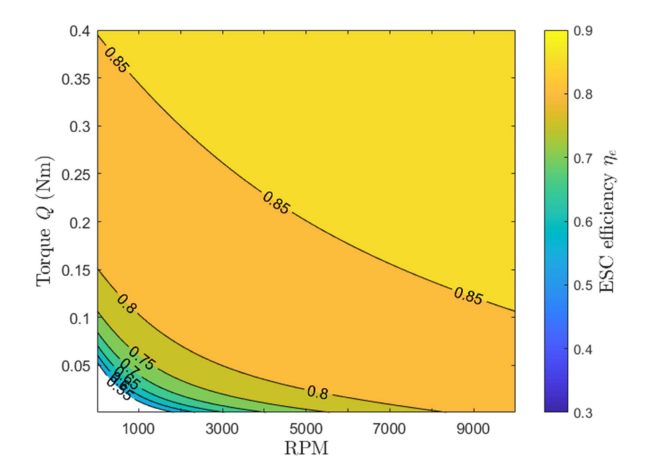


Fig. 9. Efficiency map of the "SuperBrain40" ESC with the LBM the "AT2312-1150KV" motor in the  $\omega$ -Q plane.

In addition, the efficiency value itself stays close to 85% in those regions and is not sensitive to Q or  $\omega$ .

Saemi and Benedict [8] proposed an analytical ESC efficiency model that accounts for resistive loss ( $P_{rc} = 2i_m^2 R_{ds,ON}$ ), switching loss ( $P_{sw} = f_{PWM} T_{sd} i_m v_b$ ), and harmonic loss due to throttle modulation, and is expressed as in the following:

$$\eta_e = \frac{P_{m,\text{in}}}{P_{m,\text{in}} + (P_{rc} + P_{sw})/r_D + P_{sb}}.$$
 (14)

The harmonic loss is adjusted through  $r_D$  in (7). In addition,  $R_{ds,ON}$ ,  $f_{PWM}$ ,  $T_{sd}$ , and  $P_{sb}$  are specifications that must be provided by the ESC manufacturer, representing switch resistance, pulsewidth modulation frequency, switching delay, and standby power, respectively. Fig. 10 shows the ESC efficiency contours in the  $\omega$ -Q plane using the same motor as the two previous cases. For the ESC model,  $R_{ds,ON} = 1 \text{ m}\Omega$ ,  $f_{PWM} = 12 \text{ kHz}$ ,  $T_{sd} = 200 \text{ ns}$ , and  $P_{sb} = 0.5 \text{ W}$  are used. As these parameters are not specific to the "SuperBrain40" ESC used for the two previous cases, direct comparison is not possible, however, Fig. 10 shows that the efficiency is almost constant once the  $\omega$  is above a certain threshold and has little dependency on the Q. In addition, not many COTS

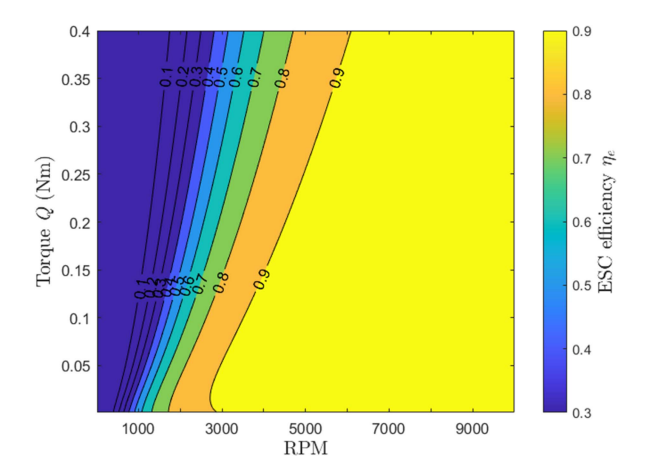


Fig. 10. Efficiency map of Saemi's ESC model [8] with the EECM of the "AT2312-1150KV" motor in the  $\omega$ -Q plane.

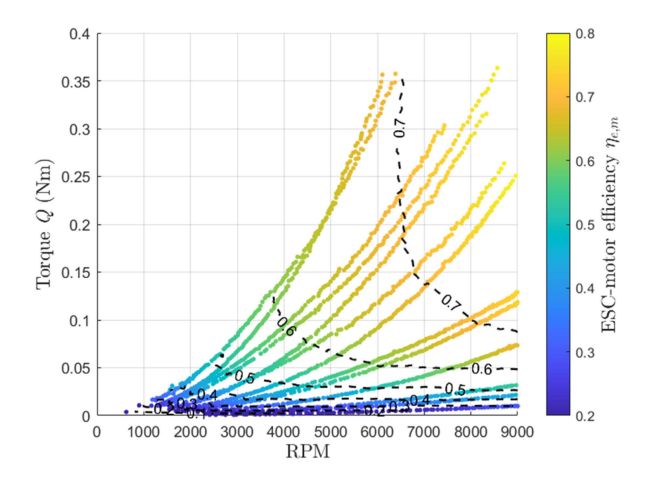


Fig. 11. Measurement data of "AT 40 A" ESC and "AT2826-900KV" motor. [11].

hobby grade ESC manufacturers provide the four parameter that are required to use this ESC model.

The three ESC efficiency maps shown in this section suggest that it may not be feasible to obtain a dependable ESC efficiency model for the design phase, and assuming a constant ESC efficiency can be sufficient, especially when the higher efficiency regions are the main concern. It is further discussed in the following section where the combined ESC-motor efficiency is investigated.

#### C. Combined ESC-Motor Efficiency

Combined ESC-motor efficiency,  $\eta_{e-m}$ , can be measured by dividing the motor output power with the ESC input power as in (15) using a low cost measurement device such as "TYTO ROBOTICS Series 1580" shown in Fig. 25. Using multiple propellers to explore the wider  $\omega$ -Q plane is used by [10] and [11].

$$\eta_{e-m} = \eta_e \eta_m = \frac{Q\omega}{v_b i_b}.$$
 (15)

Fig. 11 presents the integrated efficiency measurements of the "AT 40 A" ESC and the "AT2826-900KV" motor using 13 different propellers [11]. From the data, efficiency

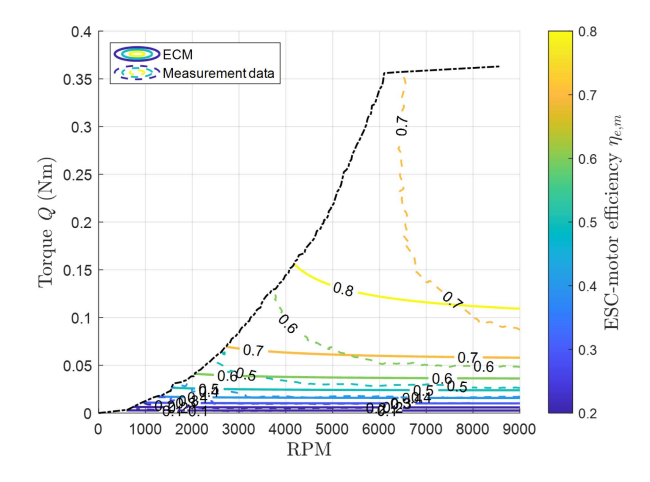


Fig. 12. Comparison of ESC-motor integrated measurement data and motor efficiency map with ECM.

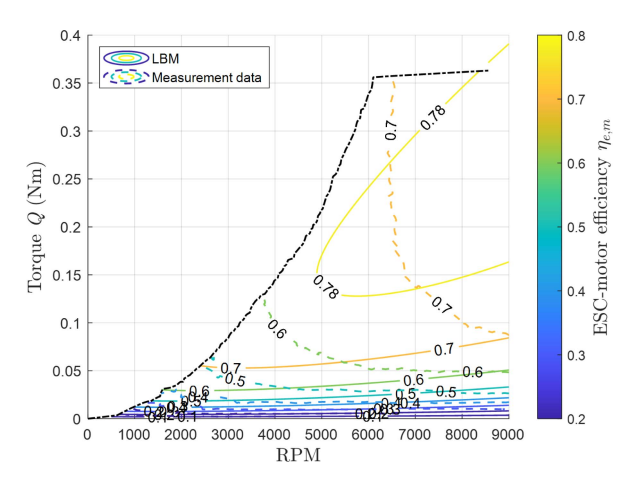


Fig. 13. Comparison of ESC-motor integrated measurement data and motor efficiency map with LBM.

contours, as depicted by the black dashed lines, can be derived.

As described in Section II, the efficiency of the ESC within the operational range of the actual electric propulsion system remains relatively constant, varying between 80% and 90%. Therefore, even when the ESC-motor integrated efficiency contours are represented using only the motor model, the overall trend remains similar, with only minor variations in efficiency depending on the specific ESC used. Figs. 12 to 14 compare the actual measured ESC-motor combined efficiency from Fig. 11 with the motor models, ECM, LBM, and EECM, respectively. As shown in Fig. 14, despite being compared to the ESC-motor integrated efficiency contours, the EECM model conservatively underestimates motor efficiency compared to the actual measured data. However, among the three motor models, the EECM exhibits the most similar trend. Consequently, in this study, in situations where ESC-motor integrated measurement data were unavailable, the EECM was utilized as a substitute to approximate the ESC-motor integrated efficiency contours.

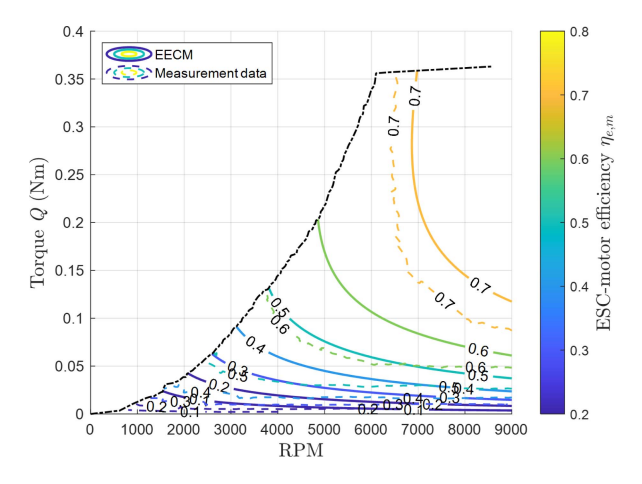


Fig. 14. Comparison of ESC-motor integrated measurement data and motor efficiency map with EECM.

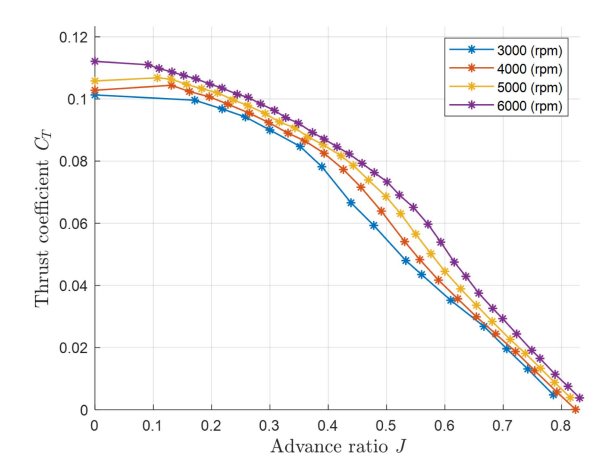


Fig. 15. Thrust coefficient measurement data for "APC sport 11x8" propeller [26].

## D. Propeller

The propeller efficiency,  $\eta_P$ , can be expressed, as shown in (16), as the ratio of the product of thrust,  $\mathcal{T}$ , and the forward flight speed, V, to the power output from the motor. In addition, the propeller efficiency can also be expressed in terms of the nondimensional coefficients: the advance ratio, J, thrust coefficient,  $C_T$ , and power coefficient,  $C_P$ 

$$\eta_p = \frac{P_{p,\text{out}}}{P_{p,\text{in}}} = \frac{TV}{Q\omega} = J\frac{C_T}{C_P}.$$
 (16)

The  $C_T$  and  $C_P$  of a propeller are primarily functions J with a secondary dependency on  $\omega$  due to the Reynolds number effect. Propeller data can be obtained from propeller analysis tools, such as XROTOR [24] or JavaPROP [25], or from wind tunnel measurements. Figs. 15 to 17 show the  $C_T$ ,  $C_P$ , and  $\eta_P$  curves of the "APC Sport 11x8" propeller, based on the wind tunnel test data provided by the UIUC propeller data site [26].

On the  $\omega$ -Q plane, since the power input to the propeller is known from the motor output, the power coefficient  $C_P$  can be calculated using the following, based on the air density,  $\rho$ , rotational speed, n, in revolutions per second,

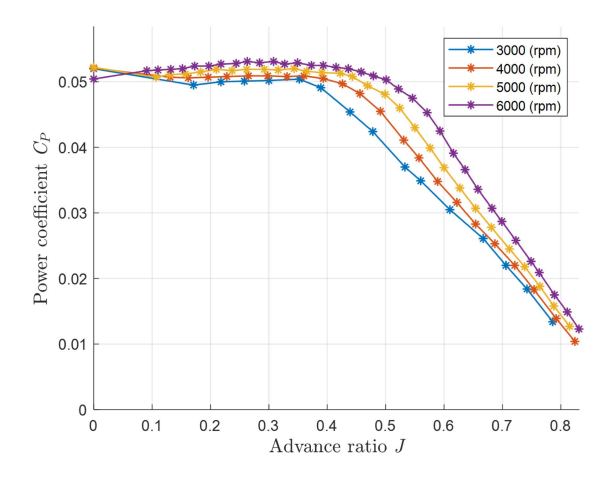


Fig. 16. Power coefficient measurement data for "APC sport 11x8" propeller [26].

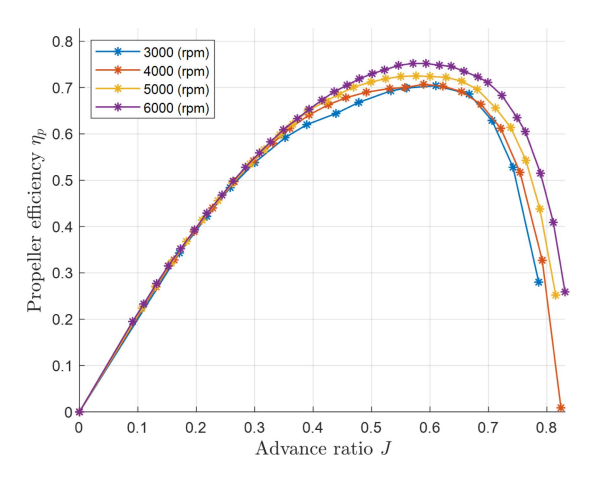


Fig. 17. Efficiency measurement data for "APC sport 11x8" propeller [26].

and the propeller diameter, D:

$$C_P = \frac{P_{p,in}}{\rho n^3 D^5}. (17)$$

The value of J, corresponding to the calculated  $C_P$  from  $\omega$  and (17), can be obtained from propeller measurement data or from a  $C_P$  curve generated using a propeller analysis tool. In exceptional cases, where J is relatively small, the  $C_P$  may not be a one-to-one match with J. As illustrated in Fig. 17, for a range of low J values, the larger the J, the more efficient the propeller. Accordingly, employing the largest J value that correlates with the corresponding  $C_P$  value and expressing it in the  $\omega$ -Q plane will facilitate the identification of the optimal electric propulsion system efficiency.

Once the J is identified, the  $C_T$  corresponding to this J and  $\omega$  is obtained from the propeller data. The thrust,  $\mathcal{T}$ , and V can be calculated from (18) and (19), respectively. One of the notable points in the proposed methodology is represented in (19) where V is not an input but an output at each grid point when constructing the contours

$$\mathcal{T} = C_T(J, \omega)\rho n^2 D^4 \tag{18}$$

$$V = JnD. (19)$$

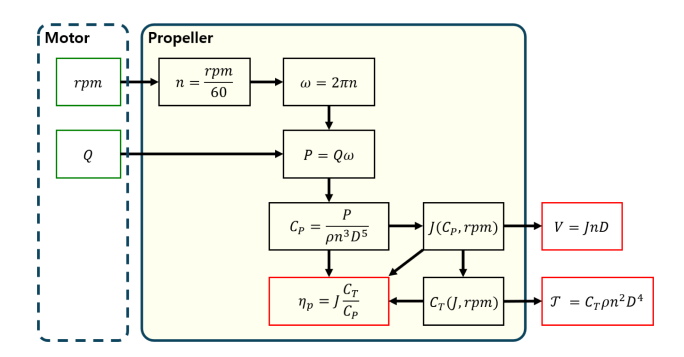


Fig. 18. Procedure for calculating propeller efficiency and performance.

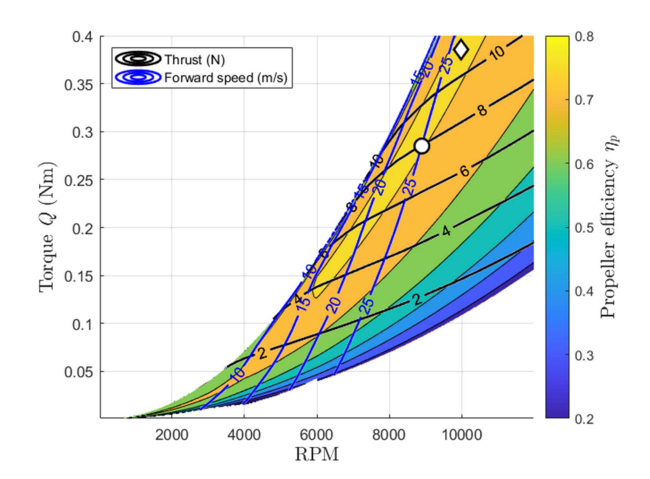


Fig. 19. Efficiency map and performance contours of the "APC Sport 11x8" propeller on the  $\omega$ -Q plane.

Fig. 18 provides a summary of the process of plotting the efficiency and performance of the propeller on the  $\omega$ -Q plane, based on the propeller data.

Fig. 19 illustrates the propeller efficiency map and performance contours on the  $\omega$ -Q plane, calculated using the data for 3000 to 6000 r/min presented in Figs. 15–17 provided in [26] and the aforementioned process. In this representation, regions where the propeller's rotational speed is lower than 3000 r/min were represented using the 3000 r/min data, while regions higher than 6000 r/min were represented using the 6000 r/min data. As  $C_T$  and  $C_P$  depend primarily on J, and the dependence on rpm represents smaller Reynolds number effects [27], substituting higher rpm regions with lower rpm data only makes the prediction slightly conservative, as discussed in [21].

In Fig. 19, The propeller efficiency is the highest at around 75.3% in the region marked by the white rhombus, which is shown inside the narrow yellow region that extends from the bottom left (rpm = 6000, Q = 0.15 N·m) to top right (rpm = 9000, Q = 0.35 N·m). For example, at the data point at which the contours V = 25 m/s and T = 8 N intersect, marked by the white circle, the  $\omega$  is around 8900 r/min and Q is around 0.29 N·m. As previously mentioned, the V and T become the link to the airframe, which is the final component of the system,

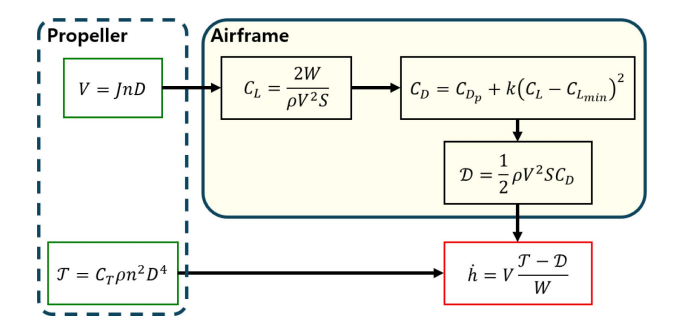


Fig. 20. Procedure for calculating the climb rate based on the given propeller performance.

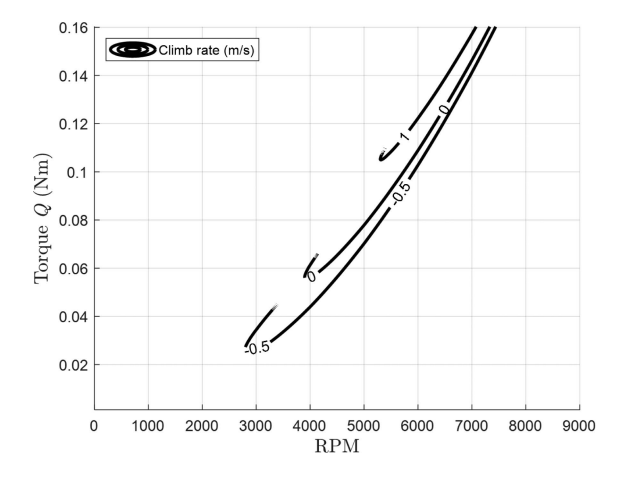


Fig. 21. Climb rate contours in the  $\omega$ -Q plane.

#### E. Airframe and Performance

Weight, W, wing area, S, and the drag model are required from the airframe side. The drag model, which is referred to as a drag polar, can usually be represented by the quadratic relation in (20). However, a lookup table based on higher fidelity simulations or wind tunnel test can be used. In (20),  $C_{D_P}$  is the parasite drag coefficient, k is the overall induced drag factor,  $C_D$  is the total drag coefficient, and  $C_{L_{\min}}$  is the lift coefficient at which the drag coefficient is minimum. The parameter k includes the contribution of the lift dependent viscous drag as well as the the induced drag. The drag,  $\mathcal{D}$ , is calculated using (21)

$$C_D = C_{D_P} + k(C_L - C_{L_{\min}})^2$$
 (20)

$$\mathcal{D} = \frac{1}{2}\rho V^2 SC_D. \tag{21}$$

The contours of the constant climb rate,  $\dot{h}$ , computed using (22) are plotted for the airframe. This process is summarized in Fig. 20. V is an output from the propeller model and determines the  $C_L$ , which leads to a fixed  $\mathcal{D}$ .  $\mathcal{T}$  is also an input from the propeller. Instead of attempting to match the  $\mathcal{T}$  and  $\mathcal{D}$ , calculating  $\dot{h}$  is one of the crucial enablers of this method [20]

$$\dot{h} = V \frac{\mathcal{T} - \mathcal{D}}{W}.$$
 (22)

Fig. 21 shows three  $\dot{h}$  contours as an example. The contour of  $\dot{h}=0$  denotes level flight where  $\mathcal{T}=\mathcal{D}$ . A

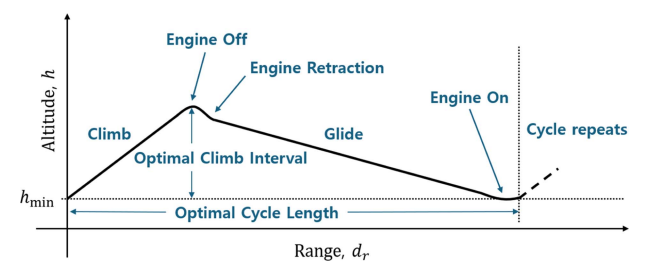


Fig. 22. Periodic flight.



Fig. 23. Airframe used in the use case.

positive  $\dot{h}$  indicates the aircraft is climbing, while a negative  $\dot{h}$  indicates the aircraft is descending.

The flight power, P, defined in (23), is the power output of the propeller to the surrounding air that provides the thrust. Total efficiency,  $\eta$ , is express as the multiplication of component efficiencies and defined by the ratio of P and the battery power,  $P_b$ , as in (24)

$$P = \mathcal{T}V \tag{23}$$

$$\eta = \frac{P}{P_b} = \eta_e \eta_m \eta_p. \tag{24}$$

If  $E_b$  is the usable energy stored in the battery, which is around 80% ~90% of the rated capacity, the endurance,  $t_E$ , is computed using (25). The level flight range,  $d_{R,level}$ , is V multiplied by  $t_E$  as in (26)

$$t_E = \frac{E_b}{P_b} = \eta \frac{E_b}{P} \tag{25}$$

$$d_{R,\text{level}} = t_E V. (26)$$

Periodic flight or saw-tooth mode is a flight that repeats the cycle of "climb," "engine OFF," "engine retraction," "glide," "engine deployment," "engine ON" [28], as shown in Fig. 22. For subsonic aircraft, it is known that periodic flights in saw-tooth mode can significantly increase range compared to level flight [29], [30]. If a simple situation where the engine ON/OFF and retraction/deployment processes are omitted and the aircraft is gliding at its maximum lift to drag ration, L/D, immediately after climb is assumed, the range can be expressed as follows:

$$d_{R,\text{periodic}} = t_E \sqrt{V^2 - \dot{h}^2} + t_E \dot{h} (L/D)_{\text{max}}. \qquad (27)$$

## III. USE CASES

In this section, the methodology proposed in the previous sections is applied to two use cases that involve maximizing the flight range,  $d_r$ , of a blended wing body style UA shown in Fig. 23. The key parameters of this UA

#### TABLE II Airframe and Flight Parameters

Parameter	Value
Span, b	1.83 (m)
Reference area, $S$	$0.59 \text{ (m}^2)$
Aspect ratio	5.6
Mean aerodynamic chord, $\bar{c}$	0.40 (m)
Total mass, $m_{total}$	2 (kg)
Battery mass, $m_b$	300 (g)
Battery capacity	4,000 (mAh)
Battery voltage, $v_b$	11.1 (V)
Static margin	9.5 (%)
Cruise $C_L$ (at trim)	0.48
Cruise speed (at trim)	10.85 (m/s)
Cruise altitude	400~600 (m)
Air density, $\rho$	1.17 (kg/m <sup>3</sup> )
Drag coefficient, $C_D$	$0.0319 + 0.0974(C_L - 0.16)^2$

TABLE III Summary of Use Cases

Models	Use Case 1	Use Case 2			
ESC-motor	In-house measurements	EECM constructed from manufacturer provided parameters (T-Motor)			
Propeller	Manufacturer provided data (APC)	Manufacturer provided data (APC)			
Airframe	In-house analysis model	In-house analysis model			
Results	Computational (Table IV)	Computational (Table VI)			

are presented in Table II. Note that the parameters are obtained from the aerodynamic analysis performed during the design process of this aircraft, not from the measurements. If measurements are made, the numerical values of  $C_{Dp}$ , k, and  $C_{L\min}$  in (20) is likely to change slightly; however, it does not impacts the methodology presented in this article. The models and measurement data of each electric propulsion component used for the two use cases are summarized in Table III.

## A. Propeller Selection for Level Flight Range Maximization

In this analysis, "AT 40 A" ESC and the "AT2312-1150KV" motor are fixed and the performance differences between eight different propellers are compared to evaluate their  $d_r$ s during a constant speed level flight. For the performance analysis, the ESC-motor integrated efficiency map, shown in Fig. 24, are used.

To generate the ESC-motor integrated efficiency map, measurements of  $v_b$ ,  $i_b$ ,  $\omega$ , and Q were collected using the "TYTO ROBOTICS Series 1580" device shown in Fig. 25 and 14 different propellers in Fig. 26.  $\eta_{e-m}$  is calculated using (15). The scattered measured data that looks similar to Fig. 11 were normalized and interpolated to a regular grid using triangulation-based linear interpolation to generate

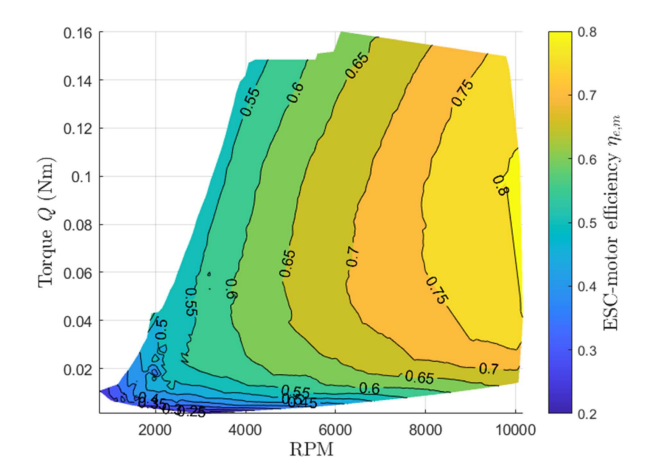


Fig. 24. ESC-motor integrated efficiency map using "AT 40 A" ESC and "AT2312-1150KV" motor measurement data.

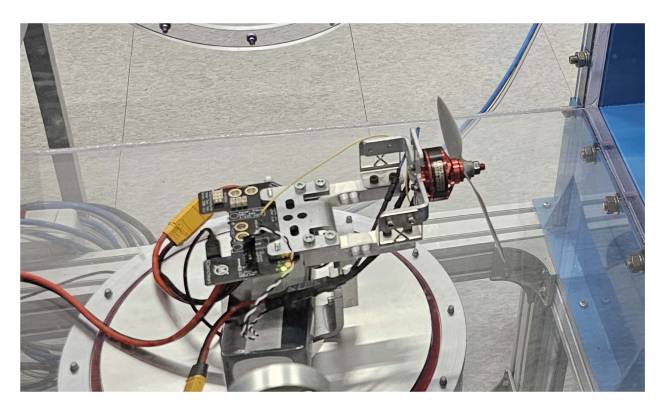


Fig. 25. Measurement device for the ESC-motor combined efficiency (TYTO ROBOTICS Series 1580).

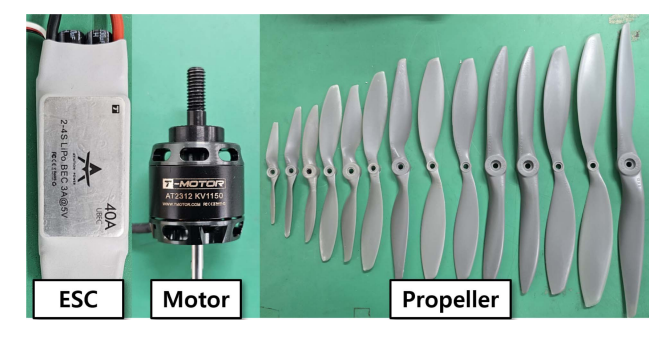


Fig. 26. System equipment used to measure ESC-motor integrated efficiency data.

smooth contours presented in Fig. 24. The actual ESC, motor, and propellers are shown in Fig. 26.

Fig. 27 presents the efficiency and performance on the  $\omega$ -Q plane for the "APC Sport 8x6" propeller, using  $C_T$  and  $C_P$  data provided by the manufacturer [31] for rpms ranging from 1000 to 10000. [31] provides data for rpms well over 20000, so the actual data that correspond to the required rpms are used. The process described in Fig. 18 was applied to generate these results. It can be observed that  $\eta_P$  larger than 70% is achieved roughly above the  $\mathcal{T}=1.5$  N contour in the black solid line and to the right side of the V=15 m/s contour in the blue solid line. Furthermore,

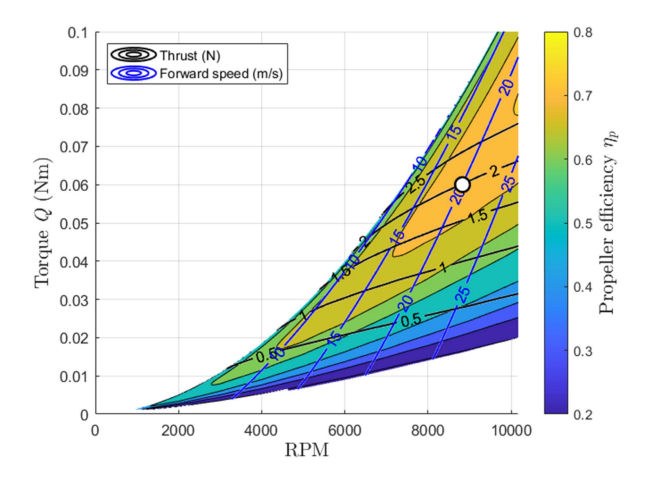


Fig. 27. Efficiency map and performance contours of the "APC Sport 8x6" propeller.

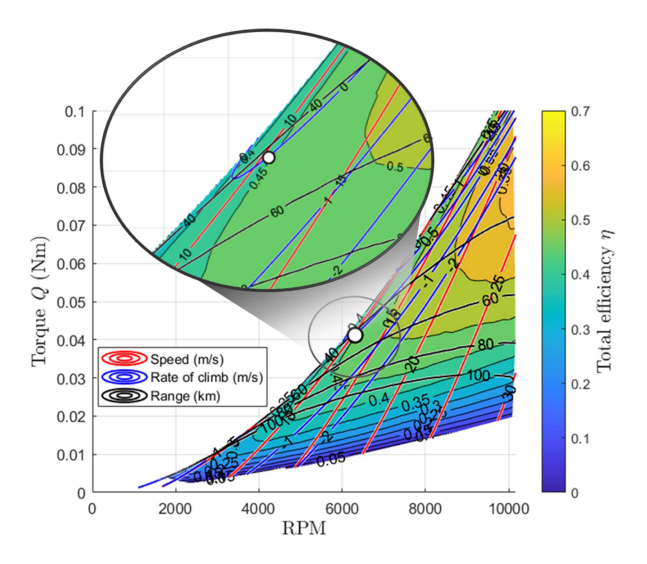


Fig. 28. Total efficiency map and performance contours.

as shown by the white circle in Fig. 27, the "APC Sport 8x6" propeller requires approximately 0.06 N·m of Q and 8800 r/min to achieve a thrust of 2N and a forward speed of 20 m/s. In comparison, "APC Sport 11x8" propeller requires approximately 0.09 N·m of torque and 6100 r/min, which can be seen in Fig. 19, to deliver the same thrust. This comparison numerically and visually demonstrates the intuitive understanding that a smaller propeller requires less torque but a higher rotational speed to achieve the same performance.

Fig. 28 shows the total efficiency ( $\eta = \eta_{e-m}\eta_p$ ),  $\dot{h}$ ,  $d_r$ , and V contours on the  $\omega$ -Q plane when the "APC Sport 8x6" propeller is combined with the given ESC and the motor. The white circle in Fig. 28 represents the maximum  $d_r$  point of this UA in level flight where  $\dot{h}$  is zero. The magnified view shows that the  $\dot{h}=0$  m/s contour intersects with the  $d_r=40$  km contour at two points. The white circle is the point on  $\dot{h}=0$  that is closest to the  $d_r=60$  km contour, which represents the maximum  $d_r$ . Note that once this point is identified, all the other performance parameters including  $\mathcal{T}$ , V,  $C_L$  as well as the individual  $\eta_{e-m}$  and  $\eta_p$  can be determined.

Fig. 28 shows that the  $\dot{h}$  contours that pass through the region where the  $\eta_{e-m}$  is high are the ones represent descent at higher Vs, which suggests that the  $\mathcal{T}$  is smaller than  $\mathcal{D}$  when the system efficiency is high. In terms of the  $\eta_{e-m}$ , the  $\dot{h}=0$  contour is almost squeezed at the upper boundary of the map, which suggests that the level flight condition requires larger than ideal torque from the given motor. Consequently, the maps can reveal that the given choice of ESC and motor may not be the best for the given airframe.

Table IV lists the computed operational points that achieve the maximum level flight  $d_r$  for all eight propellers. It can be observed that the optimal operating points change depending on the propeller. The longest  $d_r$  of approximately 43.5 km is achieved with the "APC Sport 8x6" propeller, with a system efficiency of 43.5%. In contrast, the "APC Sport 12x10" propeller yielded the lowest  $d_r$  of 38.3 km and the lowest system efficiency of 38.9%. The range difference of 5.2 km is about 13%, which can be significant depending on the mission of the aircraft.

It should be noted that the maximum L/D of 11.85 is achieved with "APC Sport 11x7." The maximum  $\eta_{e-m}$  of 72. 46% is obtained with "APC Sport 7x5." And, a maximum  $\eta_p$  of 71.46% is achieved with "APC Sport 12x10." However, the overall maximum range is achieved with a different propeller.

The results presented in Table IV signify the importance of the propulsion system analysis, because even though larger propellers spinning at smaller  $\omega$  are more efficient, smaller and faster spinning propellers result in better overall performances due to the larger gain in the ESC-motor combined efficiency.

## B. Flight Strategy for Maximum Periodic Flight Range

In this analysis,  $d_r$ s of the UA using two different motorpropeller combinations and two different flight strategies are compared. The first electric propulsion system configuration uses the "AT2321-950KV" motor model paired with the "APC Sport 8x4" propeller. The second configuration employs the "AT2826-900KV" motor model with the "APC Slow Flyer 8x4" propeller. The specifications of each motor, as provided by the manufacturer [22], are summarized in Table V, and these parameters are used to construct the EECMs as the ESC-motor combined efficiencies. In addition, the performance data of the propellers used in this analysis are based on the data provided by the manufacturer [31].

Figs. 29 and 30 illustrate the comprehensive efficiency contours of the electric propulsion system for Configuration 1 and Configuration 2, respectively. Periodic flight range contours are added in yellow color. In each figure, the point marked with a white circle represents the operational point with the maximum  $d_r$  in level flight, while the point marked with a yellow rhombus represents the operational point with the maximum  $d_r$  in periodic flight. The values of the key parameters for each operational point presented in Figs. 29 and 30 are summarized in Table VI.

TABLE IV

Computed Performance Parameters for Maximum Range in Level Flight

Propeller	rpm	Q(Nm)	$\mathcal{T}(N)$	V(m/s)	$C_L$	L/D	$d_r(\mathbf{m})$	$\eta_{e-m}(\%)$	$\eta_p(\%)$	$\eta(\%)$
APC Sport 12x10	3047	0.074	1.65	10.26	0.54	11.78	38 269	54.48	71.46	38.92
APC Sport 12x8	3424	0.068	1.64	10.15	0.55	11.81	38 572	57.40	68.16	39.12
APC Sport 11x7	3972	0.059	1.64	9.99	0.57	11.85	40 450	61.18	66.81	40.87
APC Sport 10x8	4189	0.059	1.67	10.63	0.50	11.62	41 531	62.11	68.94	42.82
APC Sport 9x8	4727	0.053	1.67	10.61	0.50	11.63	42 498	64.45	67.91	43.77
APC Sport 8x7	5916	0.044	1.68	11.61	0.50	11.61	43 408	68.67	65.37	44.89
APC Sport 8x6	6312	0.041	1.66	10.53	0.51	11.68	43 488	69.45	64.34	43.49
APC Sport 7x5	8020	0.034	1.67	10.56	0.51	11.66	43 354	72.46	61.51	44.57

TABLE V Motor Manufacturer Provided Data

Parameter	AT2321-950KV	AT2826-900KV
No-load current, $i_0$	1.2 (A)	2.2 (A)
Internal resistance, $r$	$0.065 \; (\Omega)$	$0.024~(\Omega)$
Torque constant, $k_t$	0.0101 (Vs)	0.0106 (Vs)

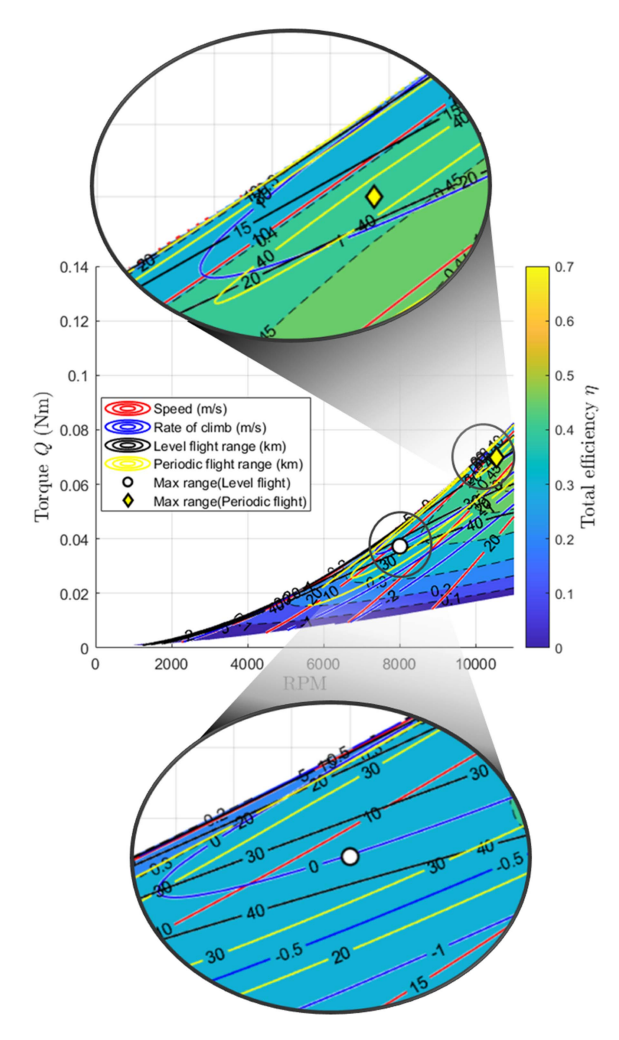


Fig. 29. Total efficiency map and performance contours for Configuration 1.

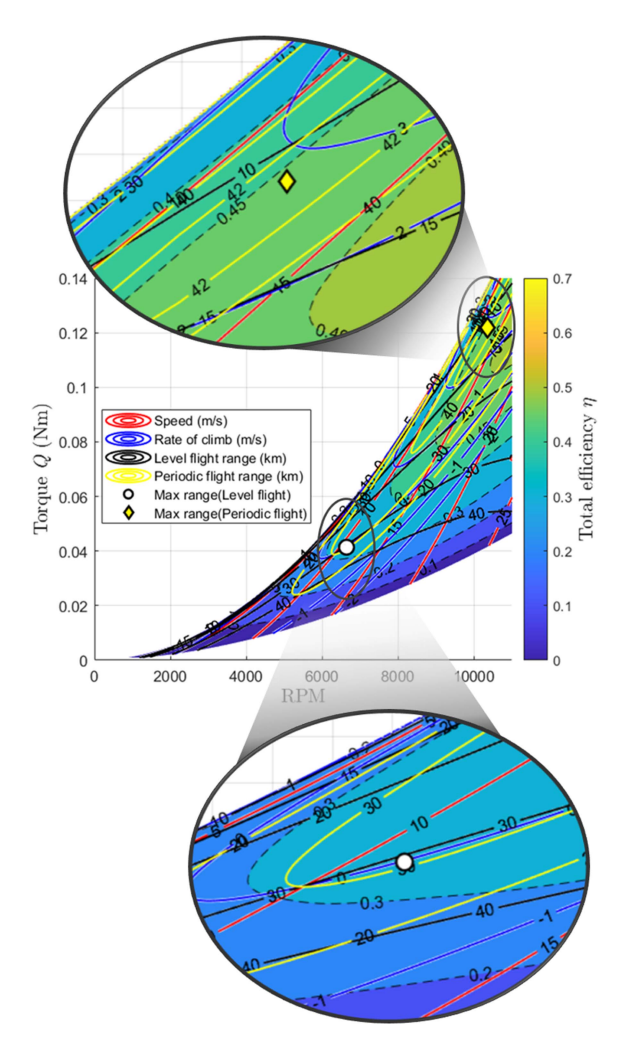


Fig. 30. Total efficiency map and performance contours for Configuration 2.

The results presented in Table VI demonstrate that the optimal operating point for a given combination of electric propulsion systems can vary significantly depending on the flight strategy. The maximum  $d_r$  of the Configuration 1 in level flight is 35.7 km, with an overall system efficiency of 37.5%, while the maximum  $d_r$  in periodic flight is 40.35 km, and the overall system efficiency is 42.9%.

TABLE VI Computed Performance Parameters for Maximum Range

	$P_b(\mathbf{W})$	rpm	Q(Nm)	$\mathcal{T}(N)$	V(m/s)	$C_L$	L/D	$\dot{h}$ (m/s)	$d_r(\mathbf{m})$	$\eta_{e-m}(\%)$	$\eta_p(\%)$	$\eta(\%)$
Configuration 1 (Level flight)	49.76	8 000	0.037	1.70	10.98	0.47	11.42	0	35 742	62.80	59.75	37.52
Configuration 1 (Periodic flight)	102.73	10 550	0.070	3.79	11.64	0.42	10.91	1.18	40 354	75.28	57.03	42.93
Configuration 2 (Level flight)	57.43	6 640	0.041	1.70	10.96	0.47	11.43	0	30 911	50.13	64.66	32.41
Configuration 2 (Periodic flight)	175.26	10 350	0.122	6.40	12.55	0.36	10.06	2.85	42 502	75.45	60.72	45.81

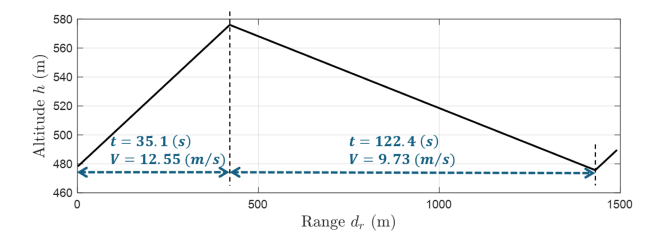


Fig. 31. Flight profile for the periodic flight of Configuration 2.

Similarly, in Configuration 2, the level flight  $d_r$  of 30.91 km is smaller than that of Configuration 1, but the periodic flight  $d_r$  of 42.5 km is larger than that of Configuration 1. From Table VI, it can be observed that Configuration 1 has the larger total efficiency of 37.5% at level flight condition, but Configuration 2 has larger efficiency of 45.8% at the maximum periodic flight condition, which resulted in the largest  $d_r$  in the periodic flight. Figs. 29 and 30 show that the two optimal operating conditions for level and periodic flight, respectively, in Configuration 1 are closer together than those in Configuration 2. It should be noted that the operating points for the maximum periodic flight  $d_r$  s are not the maximum efficiency conditions. Fig. 31 shows the climb and descent profile assuming a 100 m climb for the periodic flight of Configuration 2.

The results suggest that if the selection of the propulsion components are limited, it is possible to increased the performance by changing the flight strategy or the mission profile.

#### IV. CONCLUSION

This article presents a methodology for analyzing an electric propulsion system as a whole, starting with the efficiency of each component and ending with the overall system efficiency over a wide range of operating conditions. Rotational speed and torque of the motor are identified as the two independent variables. The article shows how to draw and interpret the efficiency and other essential performance contours on a single plot. For each component of the system, it is shown how efficiency maps can be obtained from either models utilizing commonly available data or from measurement data. The use of measurement data provides a more accurate system efficiency map, while the use of models allows for a quick relative comparison of the performance of different system combinations.

This methodology can be used in the design phase of an aircraft or to select the optimal electric propulsion components for an existing aircraft. The latter of the two, presented as a use case in this article, shows that the range can vary by more than 13% depending on the propeller, even when using the same ESC and motor. The second use case demonstrates that the maximum level flight range operating point and maximum efficiency operating point can be identified on the map, and different mission strategy can be employed to extend the range of the aircraft.

In summary, this article developed a methodology that provides the total view of the selected propulsion components. The aircraft designers will have a comprehensive view of the total and individual component and will be able to identify the necessary design changes including modification to flight strategies or missions. Finally, by unifying the independent variables to rational speed and torque, when an optimizer or solver based approach is utilized, the results can be verified through the maps, which contributes to the reliability of the design.

#### REFERENCES

- [1] C. Hwang, "Status and challenges of urban air mobility development," *Curr. Ind. Technological Trends Aerosp.*, vol. 16, no. 1, pp. 33–41, 2018.
- [2] B. Zhang, Z. Song, F. Zhao, and C. Liu, "Overview of propulsion systems for unmanned aerial vehicles," *Energies*, vol. 15, no. 2, pp. 455–474, 2022.
- [3] J. S. Langford and D. K. Hall, "Electrified aircraft propulsion," *Bridge*, vol. 50, no. 2, pp. 21–27, 2020.
- [4] A. Gong and D. Verstraete, "Experimental testing of electronic speed controllers for UAVs," in *Proc. 53rd AIAA/SAE/ASEE Joint Propulsion Conf.*, 2017, Art. no. 4955, doi: 10.2514/6.2017-4955.
- [5] M. Drela, "First-order dc electric motor model," Massachusetts Inst. Technol., 2007, [Online]. Available: http://web.mit.edu/drela/ Public/web/qprop/motor1theory.pdf
- [6] W. Johnson, "NDARC-NASA design and analysis of rotorcraft," NASA Ames Res. Center, Moffett Field, CA, USA, Tech. Rep. NASA/TP-2009-215402, 2015. [Online]. Available: https://ntrs.nasa.gov/citations/20150021267
- [7] J. Larminie and J. Lowry, in Proc. Electric Vehicle Technol. Explained, 2012, pp. 153–155.
- [8] F. Saemi and M. Benedict, "Flight-validated electric powertrain efficiency models for small UASs," *Aerospace*, vol. 11, no. 1, 2024, doi: 10.3390/aerospace11010016.
- [9] R. McDonald, "Electric motor modeling for conceptual air-craft design," in *Proc. 51st AIAA Aerosp. Sci. Meeting New Horiz. Forum Aerosp. Expo.*, 2013, Art. no. AIAA 2013-0941, doi: 10.2514/6.2013-941.

- [10] D. Muzar and E. Lanteigne, "Experimental characterization of brushless dc motors and propellers for flight application," in *Proc. Can. Soc. Mech. Eng. Int. Congr.*, 2016, doi: 10.20381/ruor-20291.
- [11] S. Lee, H. Hwang, H.-S. Nam, and H.-T. Lee, "Analysis of combined motor and electronic speed control efficiency using contour plots," *J. Adv. Navigation Technol.*, vol. 27, no. 2, pp. 214–220, 2023.
- [12] L. W. Traub, "Range and endurance estimates for battery-powered aircraft," *J. Aircr.*, vol. 48, no. 2, pp. 703–707, 2011.
- [13] H.-S. Nam, S. Lee, H.-T. Lee, H.-G. Lee, and K.-J. Lee, "Electric propulsion system analysis and optimization for multi-rotor drones," in *Proc. IEEE Aerosp. Conf.*. IEEE, 2024, pp. 1–8.
- [14] D. Duan, Z. Wang, Q. Wang, and J. Li, "Research on integrated optimization design method of high-efficiency motor propeller system for UAVs with multi-states," *IEEE Access*, vol. 8, pp. 165432–165443, 2020.
- [15] X. Dai, Q. Quan, J. Ren, and K.-Y. Cai, "An analytical designoptimization method for electric propulsion systems of multicopter UAVs with desired hovering endurance," *IEEE/ASME Trans. Mechatron.*, vol. 24, no. 1, pp. 228–239, Feb. 2019.
- [16] R. MacNeill, D. Verstraete, and A. Gong, "Optimisation of propellers for UAV powertrains," in *Proc. 53rd AIAA/SAE/ASEE Joint Propul*sion Conf., 2017, Art. no. 5090.
- [17] H. Zhang, B. Song, F. Li, and J. Xuan, "Multidisciplinary design optimization of an electric propulsion system of a hybrid UAV considering wind disturbance rejection capability in the quadrotor mode," *Aerosp. Sci. Technol.*, vol. 110, 2021, Art. no. 106372.
- [18] R. A. McDonald, "Modeling of electric motor driven propellers for conceptual aircraft design," in *Proc. 53rd AIAA Aerosp. Sci. Meeting*, 2015, Art. no. AIAA 2015-1676, doi: 10.2514/6.2015-1676.
- [19] A. Gong, R. MacNeill, and D. Verstraete, "Performance testing and modeling of a brushless dc motor, electronic speed controller and propeller for a small UAV application," in *Proc. Joint Propulsion Conf.*, 2018, pp. 2018–4584, doi: 10.2514/6.2018-4584.
- [20] H.-T. Lee, "A technique for matching propeller, motor, and air-frame of an electric powered aircraft based on efficiency maps," in *Proc. AIAA SCITECH Forum*, 2022, Art. no. AIAA 2022-0885, doi: 10.2514/6.2022-0885.
- [21] H.-S. Nam, H.-S. Hwang, S.-H. Lee, and H.-T. Lee, "Electric propulsion system optimization using performance maps," in *Proc. IEEE Aerosp. Conf.*, 2023, pp. 1–8.
- [22] M. Wu, "T-motor official website," Accessed: Sep. 28, 2018. [On-line]. Available: http://store-en.tmotor.com/
- [23] R. A. McDonald, "Electric propulsion modeling for conceptual aircraft design," in *Proc. 52nd Aerosp. Sci. Meeting*, 2014, Art. no. 0 536.
- [24] M. Drela and H. Youngren, "Xrotor user guide," Massachusetts Inst. Technol., Cambridge, MA, USA, Tech. Rep., 2002. [Online]. Available: https://web.mit.edu/drela/Public/web/xrotor/xrotor\_doc.txt
- [25] M. Hepperle, "Javaprop users guide," 2010. [Online]. Available: https://www.mhaerotools.de/airfoils/javaprop.htm
- [26] J. B. Brandt, R. W. Deters, G. K. Ananda, O. D. Dantsker, and M. S. Selig, "Uiuc propeller database," 2020. [Online]. Available: https://m-selig.ae.illinois.edu/props/propDB.html
- [27] R. W. Deters, G. K. Ananda Krishnan, and M. S. Selig, "Reynolds number effects on the performance of small-scale propellers," in *Proc. 32nd AIAA Appl. Aerodynamics Conf.*, 2014, Art. no. 2151.

- [28] J. Lenz, "Optimisation of periodic flight trajectories," Ph.D. dissertation, MAS Maschinenbau, Technische Universität München, Munich, Germany, 2015. [Online]. Available: https://mediatum.ub.tum.de/1237119
- [29] R. H. Chen and J. L. Speyer, "Improved endurance of optimal periodic flight," *J. Guidance, Control, Dyn.*, vol. 30, no. 4, pp. 1123–1133, 2007.
- [30] G. Sachs, J. Lenz, and F. Holzapfel, "Range maximization by saw-tooth mode optimization for motor gliders with retractable engines," *Tech. Soaring*, vol. 34, no. 4, pp. 68–74, 2010.
- [31] APC Propellers, "Performance data of APC propellers," Accessed: Oct. 10, 2024. [Online]. Available: https://www.apcprop.com/technical-information/performance-data/



Hong-Su Nam received the B.S. degree in aerospace engineering in 2021 from Inha University, Incheon, Republic of Korea, where he is currently working toward the Ph.D. degree with Aerospace Control and Systems Laboratory, Department of Aerospace Engineering and Program in Aerospace Systems Convergence. His research topics inlude design optimization of electric aircraft, aircraft performance data analysis.



**Seok-Hwan Lee** received the B.S. degree in aerospace engineering in 2022 from Inha University, Incheon, Republic of Korea, where he is currently working toward the M.S. degree with Aerospace Control and Systems Laboratory, Department of Aerospace Engineering and the Program in Aerospace Systems Convergence.

His research interest includes the processing and analysis of flight data and the optimization of electric propulsion system.



**Hak-Tae Lee** received the Ph.D. degree in aeronautics and astronautics from Stanford University, Stanford, CA, USA, in 2006.

He is currently a Professor with the Department of Aerospace Engineering and the Program in Aerospace Systems Convergence, Inha University, Incheon, Republic of Korea. Prior to joining Inha University, he conducted research with the Aviation Systems Division, NASA Ames Research Center. At NASA, he worked on large-scale simulations of current commercial

air traffic with future unmanned aircraft (UA) operations. He also developed a fast and effective scheduler that can handle complicated constraints to conduct traffic flow management studies. His research interests include air traffic management (ATM), which aims to improve aircraft operations, and aircraft design, especially electric propulsion systems and UA.